Properties of magnetic sublevel coherences for precision measurements

I. Chan, A. Andreyuk, S. Beattie, B. Barrett, C. Mok, M. Weel, and A. Kumarakrishnan
Department of Physics and Astronomy, York University, 4700 Keele, Toronto, Ontario, Canada M3J 1P3
(Received 26 June 2008; published 17 September 2008)

We have developed a theoretical description of the evolution of ground state coherences between magnetic sublevels in Rb vapor in the presence of a magnetic field along an arbitrary direction. This formalism uses a rotation matrix approach to describe the evolution of coherences created by two traveling wave laser pulses with orthogonal polarizations. The effect of a magnetic field can be described as a time-dependent rotation of the atomic system about the quantization axis. Predictions based on this theoretical formalism for the functional form of Larmor oscillations in a magnetic field are studied using a coherent transient effect known as magnetic grating free induction decay (MGFID) using room temperature vapor and laser cooled atoms. We find the theoretical predictions to be in excellent agreement with data. The velocity distribution of the cold sample measured from the dephasing time of the MGFID in the absence of magnetic fields is in agreement with the sample temperature obtained by imaging the ballistic expansion of the trapped cloud. By using rate equations to model atomic coherences, it is also possible to predict the evolution of magnetic grating echoes (MGE) in a magnetic field. We compare these predictions with experiments from cold atoms and discuss applications of the MGFID and MGE that relate to a precision measurement of the atomic g factor ratio using ^{85}Rb and ^{87}Rb isotopes.

DOI: 10.1103/PhysRevA.78.033418 PACS number(s): 42.50.Md, 82.53.Kp, 03.75.−b, 42.62.Fi

I. INTRODUCTION

Properties of atomic coherences have been exploited for interesting applications such as quantum state preparation [1] and control [2], nondemolition measurements [3,4], entanglement [5], and precision magnetometery [6]. Other interesting applications have related to studies of velocity changing collisions using both radio frequency (rf) [7] and optical excitation [8] and experiments with coherent transient effects that involve coupling between Zeeman sublevels [9,10]. The behavior of atomic coherences in static magnetic fields can also be exploited for precision measurements of the strength of magnetic interactions such as atomic g factor ratios and the Zeeman shift [11–15].

In this paper, we describe the evolution of magnetic sublevel coherences under the influence of static magnetic fields in rubidium vapor, and consider an application related to achieving an improved precision measurement of the ratio of atomic g factors in two Rb isotopes that relies on a precise measurement of the Larmor frequency ω_L. We use coherent transient effects designated as magnetic grating free induction decay (MGFID) and magnetic grating echoes (MGE) that were originally predicted in Ref. [16]. These signals involve spatially periodic coherences between magnetic sublevels of ground state atoms and their basic properties were investigated in Refs. [17,18]. The experimental work in Ref. [17] discussed the evolution of coherences for particular orientations of magnetic fields whereas Ref. [18] focused on the effect of collisions and showed that the MGE could be observed on a time scale determined by the transit time of atoms through the region of interaction.

In a static magnetic field, it is known that the Zeeman shift between magnetic sublevels causes temporal oscillations within the envelopes of these signals at multiples of ω_L [17]. In this work, we present an analytical calculation that predicts the functional form of the Larmor oscillations in the MGFID in arbitrary static magnetic fields for excitation pulses with both orthogonal linear and circular polarizations. The theoretical treatment is based on a rotation matrix approach [19–21] in which the effect of the magnetic field can be described as a time-dependent rotation of the atomic system about the quantization axis. We use data from room temperature vapor and laser cooled atoms to show that the theory accurately describes the signals observed in the experiment. In the absence of magnetic fields, we show that the velocity distribution of a cold sample measured using the MGFID is in agreement with the results of an independent technique used to measure the sample temperature. We also use rate equations outlined in Refs. [16,22,23] to understand the properties of the MGE in a magnetic field. We show that the results of simulations are in agreement with data from laser cooled atoms. An interesting aspect of these studies is that we show that the amplitude of the MGE envelope exhibits oscillations that depend on the Rabi frequencies of the excitation pulses and the magnetic field as a function of the time between excitation pulses. However, Rabi frequency oscillations average out due to the effect of the spatial profile of the excitation beam allowing magnetic field dependent oscillations to be observed. This effect can be explained in analogy with optical Bloch equations that model a two level atomic system.

The durations of the envelopes of the MGFID and MGE are related to the velocity distribution of the sample [17,18]. For a laser cooled sample, this duration is typically $\sim$1 ms. As a result, Larmor oscillations can be measured with high precision on this time scale. In this paper, we discuss measurements of the atomic g factor ratio obtained by measuring ω_L using the MGFID in two isotopes of Rb. We show that the time scale of the measurement can be extended by about a factor of 2 by recording Larmor oscillations under the MGE envelope. Since the MGE exhibits envelope amplitude oscillations, and since it should be possible to observe the MGE on a time scale comparable to the transit time of cold

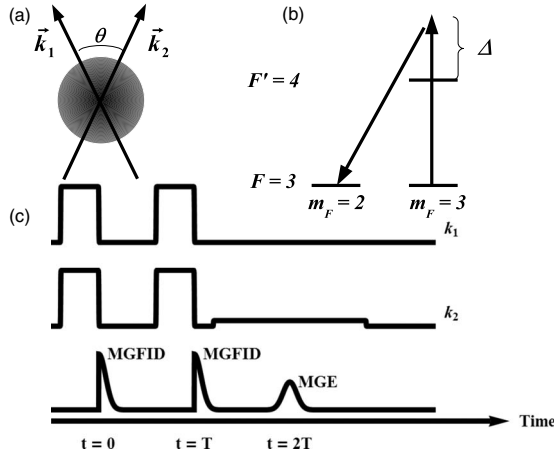

FIG. 1. (a) Laser pulses along $\vec{\mathbf{k}}_1$ and $\vec{\mathbf{k}}_2$ excite a sample of atoms (laser cooled gas, or room temperature vapor); $\theta \sim 10$ mrad (b) Level diagram for the experiment with $\vec{\mathbf{k}}_1$ and $\vec{\mathbf{k}}_2$ having orthogonal linear polarizations; $\Delta \sim 40$ MHz. (c) Timing diagram for the MGE signal.

atoms through the region of interaction (several tens of milliseconds), our results suggest that it should be possible to use the MGE to achieve a significant improvement in the precision with which the g factor ratio can be determined. We note that the goal of previous experiments in alkali-metal vapor magnetometry [24] was to carry out measurements on a suitably long time scale to avoid transit time signal decay and spin relaxation due to wall collisions.

For the experiments considered in this work, the sample of atoms is excited using two simultaneous traveling wave laser pulses applied at $t=0$ with wave vectors $\vec{\mathbf{k}}_1$ and $\vec{\mathbf{k}}_2$ at a small angle [$\theta \sim 10$ mrad, as shown in Fig. 1(a)]. The atomic sample is either Rb vapor at room temperature, or a cloud of laser cooled atoms loaded into a magneto optical trap (MOT). The individual traveling waves pulses have orthogonal linear or circular polarizations and are detuned from the excited state (in a laser cooled sample). However, the pulses are resonant with the two photon transition that couples two magnetic sublevels of the ground state as shown in Fig. 1(b). The timing diagram is shown in Fig. 1(c). The excitation creates a spatially periodic superposition between the magnetic sublevels of the ground state coupled by the laser fields. The superposition has a period of $\sim \lambda/\theta$ where λ is the wavelength of the excitation. The grating is probed by a read out pulse along $\vec{\mathbf{k}}_2$ and the resulting signal (MGFID) is coherently scattered along $\vec{\mathbf{k}}_1$ due to conservation of momentum. The grating dephases due to thermal motion of the atoms and the time scale of the signal decay (defined as the decay time) is determined by the time taken by a typical atom to move a distance on the order of a grating spacing $(\frac{\lambda}{\theta u})$, where u is the most probable speed associated with the Maxwell-Boltzmann velocity distribution.

The MGE is observed using a second set of excitation pulse at $t=T$ to rephase the coherence grating as in Fig. 1(c) [16–18]. The second pulse modifies the time dependent coefficients that describe the coherent superposition of magnetic sublevels so that the grating reforms at $t=2T$. This is analogous to the reversal of the Doppler phases of individual atoms in a traditional two pulse photon echo experiment [25]. In the absence of decoherence due to collisions and background light, the MGE amplitude should decay on a time scale determined by the transit time of atoms through the laser beams [18].

The focus of initial experimental work using echo techniques was related to observing effects due to atomic recoil [17,26–28]. The MGFID and MGE were used to verify the expected dependence of the dephasing time of the coherences on the velocity distribution of the sample [17,18,29], observing the effect of magnetic fields for particular experimental configurations [17] and studying the effects of collisions [18]. Other applications of the MGFID include measurements of the diffusion constants [30] and phase space imaging [31]. Echo techniques were also used to investigate applications related to detecting nanostructures [32–35] and depositing periodic arrays of atoms on substrates [29,34].

The rest of the paper is organized as follows. In Sec. II, we present details of the rotation matrix approach used to calculate the MGFID in static magnetic fields and outline the rate equations used to model the MGE. In Sec. III, we outline the details of the experiment. In Sec. IV, we show that the decay time of the MGFID is an accurate technique for measuring the temperature of the sample by comparing the results to an independent technique. We show that the functional form of the Larmor oscillations in the envelope of the MGFID in static magnetic fields agrees with the theoretical predictions based on the rotation matrix approach. We consider the realization of a precision measurement of atomic g factor ratios that relies on the properties of the MGFID and possible improvements in precision using the MGE.

II. THEORETICAL CONCEPTS

A. Calculation of MGFID

The action of the rotation operator in quantum mechanics is analogous to the effect of a magnetic field on an atomic system. We consider the situation in which two excitation lasers with orthogonal polarizations are used to create a spatially periodic superposition between magnetic sublevels of the same hyperfine ground state. It is possible to excite $\Delta m = 1$ and $\Delta m = 2$ coherences using Lin $\perp$ Lin and $\sigma^+\sigma^-$ pulses, respectively. The evolution of these coherences in a magnetic field resembles the evolution of particular moments (dipole, quadrupole,…) of the atom in an irreducible tensor basis. These moments are associated with the evolution of effects termed as alignment and orientation, respectively.

A technique for describing the evolution of coherences has been described in Refs. [19,20] in the context of rotation operators and by Ref. [21] in the context of precision measurements of electric dipole moments. In this treatment, the probability of the atom being in a specific coherent superposition is defined by $\langle F,m|\rho_{mm'}|F,m'\rangle$ where F and m refer to the magnetic quantum numbers of the ground state sublevels and $\rho_{mm'}$ is an element of the atomic density matrix. To calculate the probability of an atom to be in a particular atomic state in the presence of a magnetic field, we apply the rotation operator to align the quantization axis as defined by

the laser polarizations with the quantization axis as defined by the magnetic field. This involves rotating the atomic coordinate system through the Euler angles (α,β,γ) that describe rotations about each of the axes. The rotated density matrix is given by

$$\rho_{mm'}(\theta,\phi) = D^{-1}(\phi,\theta,0)\rho_{mm'}D(\phi,\theta,0) \tag{1}$$

where

$$D(\alpha,\beta,\gamma) = \exp[i\gamma\hat{J}_z]\exp[i\beta\hat{J}_y]\exp[i\alpha\hat{J}_z]. \tag{2}$$

In Eq. (1), θ and ϕ represent the polar and azimuthal angles in the new coordinate system. The application of the rotation operator D to the atomic density matrix allows the rotation of the quantization axis through all possible angles. The rotation generates a surface such that the distance from the origin to a point on the surface defined by (r,θ,ϕ) is proportional to the probability of finding the system in a particular state. We first evaluate the rotation matrix in Eq. (2) for the level structure of interest (specific angular momentum $\hat{\mathbf{J}}$). We apply the rotation operator D to the density matrix and evolve the system in time using the Hamiltonian for the magnetic interaction. The time-dependent atomic density matrix $(\rho_{mm'})$ is then transformed into an irreducible tensor basis (ρ_Q^K) using the transformation

$$\rho_Q^K = \sum_m \sum_{m'} (-1)^{F-m'}\langle F,m;F,-m'|K,Q\rangle\rho_{mm'}, \tag{3}$$

where $\langle F,m;F,-m'K,Q\rangle$ is a Clebsch-Gordan coefficient. It is particularly convenient to write the atomic density matrix in this basis since the coherence that is established by the laser pulses is proportional to the tensor elements ρ_Q^K. Using this approach, it is also possible to handle a large number of degenerate magnetic sublevels and arbitrary light polarizations as in Ref. [22].

The inverse transformation allows us to predict the state of the system in the m basis and is given by

$$\rho_{mm'} = \sum_{K=0}^{2F} \sum_{Q=-K}^{K} (-1)^{F-m'}\langle F,m;F,-m'|K,Q\rangle\rho_Q^K. \tag{4}$$

B. Calculation for $J=1/2$ atomic system

For simplicity, we consider a system with quantum number $J=1/2$ with the atoms optically pumped into the $m=1/2$ magnetic sublevel. The matrix $\exp[i\alpha\hat{J}_z]$ is given by

$$\langle m'|\exp[i\alpha\hat{J}_z]|m\rangle = \begin{pmatrix} e^{i\alpha/2} & 0 \\ 0 & e^{-i\alpha/2} \end{pmatrix}. \tag{5}$$

The expression for $\exp[i\gamma\hat{J}_z]$ can be obtained by replacing α with γ in Eq. (5). The matrix $\exp[i\beta\hat{J}_z]$ is given by Ref. [20] as

$$\begin{aligned}\langle m'|\exp[i\beta\hat{J}_z]|m\rangle &= \sqrt{\frac{(J+m')!(J-m')!}{(J+m)!(J-m)!}}\sum_{\sigma=0}^{J-m'}\nu\begin{pmatrix} J+m \\ J-m'-\sigma\end{pmatrix}\nu\begin{pmatrix} J-m \\ \sigma\end{pmatrix} \\ &\times(-1)^{J-m'-\sigma}\left(\cos\left[\frac{\beta}{2}\right]\right)^{2\sigma+m'+m}\left(\sin\left[\frac{\beta}{2}\right]\right)^{2J-2\sigma-m'-m} \\ &= \begin{pmatrix} \cos\left[\frac{\beta}{2}\right] & -\sin\left[\frac{\beta}{2}\right] \\ \sin\left[\frac{\beta}{2}\right] & \cos\left[\frac{\beta}{2}\right]\end{pmatrix},\end{aligned} \tag{6}$$

where $\nu\binom{A}{B}$ is the binomial coefficient given by $\frac{A!}{(A-B)!B!}$ and σ is a summation index. The rotation matrix in Eq. (2) can then be written as

$$\begin{aligned}D(\phi,\theta,0) &= D(0,0,0)D(0,\theta,0)D(\phi,0,0) \\ &= \begin{pmatrix} e^{i\phi/2}\cos\left[\frac{\theta}{2}\right] & -e^{-i\phi/2}\sin\left[\frac{\theta}{2}\right] \\ e^{i\phi/2}\sin\left[\frac{\theta}{2}\right] & e^{-i\phi/2}\cos\left[\frac{\theta}{2}\right]\end{pmatrix}\end{aligned} \tag{7}$$

from which the inverse matrix D^{-1} can be calculated. We substitute the matrices for D and D^{-1} into Eq. (1) to rotate the quantization axis of the system. Assuming that the atoms are initially in the state $\rho_{mm'}=\delta_{m,\frac{1}{2}}\delta_{m',\frac{1}{2}}$, the expression for $\rho_{mm'}(\theta,\phi)$ in the rotated system is given by

$$\begin{aligned}\rho_{mm'}(\theta,\phi) &= D^{-1}(\phi,\theta,0)\begin{pmatrix} 1 & 0 \\ 0 & 0\end{pmatrix}D(\phi,\theta,0) \\ &= \begin{pmatrix} \cos^2\left[\frac{\theta}{2}\right] & -\frac{1}{2}e^{-i\phi}\sin[\theta] \\ -\frac{1}{2}e^{i\phi}\sin[\theta] & \sin^2\left[\frac{\theta}{2}\right]\end{pmatrix}.\end{aligned} \tag{8}$$

We now subject the system to a magnetic field interaction described by the Hamiltonian $\hat{H}=-g_J\mu_B\vec{\mathbf{B}}\cdot\vec{\mathbf{J}}$. We consider the specific case in which the magnetic field is at an angle $\pi/2$ with respect to the z axis (quantization direction) so that the Hamiltonian becomes $\hat{H}=\omega_x\hat{J}_x+\omega_y\hat{J}_y$. Here, $\omega_k=g_J\mu_B B_k/\hbar$ is the Larmor frequency due each component of the field. The resultant Larmor frequency is given by $\omega_L=(g_J\mu_B/\hbar)\sqrt{B_x^2+B_y^2}$. The time dependence of the density matrix in Eq. (8) is given by

$$\dot{\rho}_{mm'}(\theta,\phi,t) = \frac{1}{i}[\hat{\tilde{H}},\rho_{mm'}(\theta,\phi,t)], \tag{9}$$

where $\hat{\tilde{H}}=\hat{H}/\hbar$. The solution to Eq. (9) is given by

$$\rho_{mm'}(\theta,\phi,t) = e^{-i\hat{\tilde{H}}t}\rho_{m'm}(\theta,\phi,t=0)e^{i\hat{\tilde{H}}t}. \tag{10}$$

Using the Hamiltonian for the magnetic interaction and Eq. (8), it can be shown that

$$\rho_{mm'}(\theta,\phi,t)=\frac{1}{2}\begin{pmatrix}1+\cos[\omega_L t]\cos[\theta]-\sin[\omega_L t]\sin[\theta]\cos[\phi] & \sin[\omega_L t]\cos[\theta]+\sin[\theta](\cos[\omega_L t]\cos[\phi]-i\sin[\phi])\\ \sin[\omega_L t]\cos[\theta]+\sin[\theta](\cos[\omega_L t]\cos[\phi]+i\sin[\phi]) & 1-\cos[\omega_L t]\cos[\theta]+\sin[\omega_L t]\sin[\theta]\cos[\phi]\end{pmatrix}. \tag{11}$$

The surface at $t=0$ obtained from the first matrix element in Eq. (11) is spherical and is shown in Figs. 2(a). The time evolution of the surface in Figs. 2(a)–2(d) obtained using Eq. (10) is given by the first element of the matrix in Eq. (11). From this surface, we obtain the time-dependent atomic density matrix for all possible directions of the magnetic field with respect to the atomic quantization axis. The solution for the case when the magnetic field (along $\hat{y}$) is perpendicular to the quantization axis of the atomic system (along $\hat{z}$) is obtained by substituting $\theta=0$ and $\phi=0$ into Eq. (11). For a different direction of the field, the Hamiltonian remains unchanged and only the orientation of the quantization axes has to be specified through the angles θ and ϕ.

The time evolution of the first element of the matrix in Eq. (11) is shown in Fig. 3. As the surface rotates, the distance to the surface along the quantization axis changes in a periodic manner. The vertical axis in Fig. 3 represents this distance. The time evolution of $\rho(\theta,\phi,t)$ corresponds to a precession of the dipole around the direction of the field.

C. Calculation for $F=3$ atomic system

We use the same technique described in Sec. II B to obtain ρ_Q^K [defined by Eq. (3)] as a function of time for the $F=3$ manifold in ^{85}Rb for the case in which the ground states are coupled by the traveling waves $\vec{\mathbf{k}}_1$ and $\vec{\mathbf{k}}_2$. For Lin $\perp$ Lin excitation, the tensor element that is excited by the fields is $\rho_Q^K=\delta_{K,1}\delta_{Q,1}$. Correspondingly, for this atomic system, the time dependence of the MGFID in a magnetic field is proportional to ρ_1^1. This can be calculated using Eq. (9) to be

$$\rho_1^1(t)\propto\cos[\omega_L t]+\sin[\eta]+i\cos[\eta]\sin[\omega_L t]. \tag{12}$$

Here, we use η to specify the angle between the magnetic field and the quantization axis of the atoms as defined by the laser polarizations. For $\sigma^+\sigma^-$ excitation the relevant tensor element is $\rho_Q^K=\delta_{K,2}\delta_{Q,2}$, and the time dependence in a magnetic field is given by

$$\rho_2^2(t)\propto e^{-2i(\omega_L t+\eta)}[i(1-e^{-i\eta})+e^{i\omega_L t}+e^{i(\omega_L t+\eta)}]^4. \tag{13}$$

If the magnetic field is along the direction of polarization of one of the excitation pulses ($\eta=0$), then the form of the oscillations are simple sinusoidal functions. If $\eta\neq 0$, then the time-dependent coherences predicted by these equations have multiple frequency components. In Sec. IV, we compare the predictions of Eq. (12) and (13) to results from signals obtained from a room temperature vapor cell as well as a sample of laser cooled atoms.

The results from experiment are compared to predictions by including the effect of signal decay due to Doppler dephasing, an effect that is not considered in the theoretical description. A formal derivation of the signal measured in response to a read out pulse is described in Ref. [16].

D. Calculation of MGE

In this section, we model effects associated with the MGE from trapped atoms that impact precision measurements of ω_L. We first discuss Larmor oscillations inside the MGE envelope. We then describe oscillations of the MGE envelope at $t=2T$ which are analogous to Rabi oscillations in a two

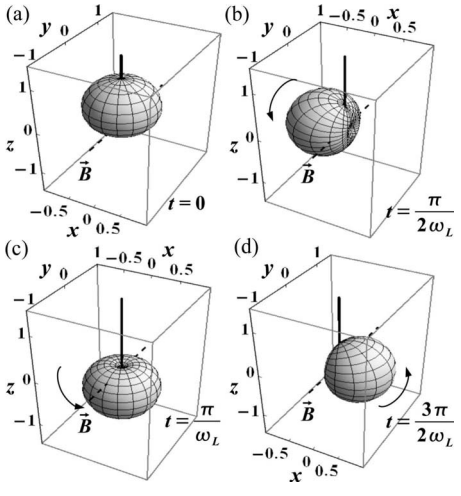

FIG. 2. We consider the situation in which the quantization axis is along $\hat{z}$ (solid black line) and the magnetic field is along $\hat{y}$ (dotted line) for an atomic system with $J=\frac{1}{2}$. (a) Surface $\rho_{1/2,1/2}(\theta,\phi,t)$ for $t=0$. (b) $\rho_{1/2,1/2}(\theta,\phi,t)$ for $t=\frac{1}{4}T_L$ (c) $\rho_{1/2,1/2}(\theta,\phi,t)$ for $t=\frac{1}{2}T_L$ (d) $\rho_{1/2,1/2}(\theta,\phi,t)$ for $t=\frac{3}{4}T_L$. Here, $T_L=2\pi/\omega_L$. The surface rotates around the direction of the magnetic field with frequency ω_L as a function of time.

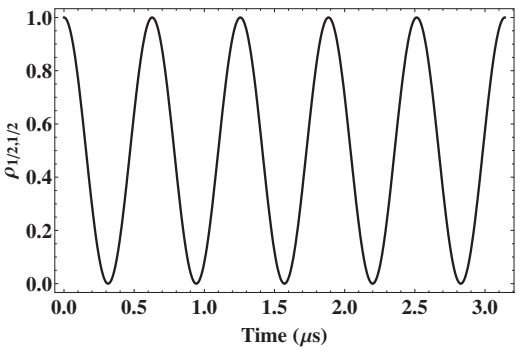

FIG. 3. Time evolution of a point on the surface shown in Fig. 2 with $(\theta,\phi)=(0,0)$. The time evolution is calculated using Eq. (10) for the surface shown in Fig. 2. The solution for $\rho_{1/2,1/2}(\theta,\phi,t)$ is given by the first element in Eq. (11). The magnetic field is in the $\hat{y}$ direction.

level system. These oscillations depend on the Rabi frequency and the magnetic field, but only the magnetic field induced oscillations are important on the time scale for which the signal is observed. Finally, we discuss the effects of magnetic field gradients on these oscillations.

The rotation matrix approach is clearly well suited to describe the MGFID in the tensor basis since it gives analytical expressions for arbitrary magnetic field directions. In contrast, the evolution of the MGE is more complicated. It requires knowledge of the evolution of the magnetic sublevel populations and coherences during both excitation pulses as well as the evolution of the Doppler and Larmor phases during the experiment.

As a result, we use numerical simulations to model the system of rate equations and calculate the MGE. The simulations solve for $\rho_{mm'}$ in the presence of a magnetic field [16]. This system of rate equations [16,22] can be applied to a multilevel atomic system excited by light fields with specific polarizations to calculate the envelope of the MGE signal shown in Fig. 1(c). Each excitation laser is detuned by $\Delta_{FF'}$ from the $F \rightarrow F'$ transition and effect of the two photon coupling is described by the parameter χ^2/Δ. Here, χ^2 is the product of the one photon Rabi frequencies χ_1 and χ_2 associated with the excitation pulses. The two laser fields with wave vectors $\vec{\mathbf{k}}_1$ and $\vec{\mathbf{k}}_2$ interact with an atom with velocity v_z. The angle between the wave vectors (θ) is small such that $|\Delta\vec{\mathbf{k}}| \simeq k\theta$. We consider the particular case in which laser fields have orthogonal linear polarizations which couple adjacent magnetic sublevels. It is assumed that $\Delta \gg \Gamma$, where $\Gamma = 3.7 \times 10^7$ s^{-1} is the radiative rate of the excited state. We also use excitation pulse widths with spectral bandwidths that are small compared to Δ. Under these conditions, the equations involving excited state populations and coherences can be neglected (a more comprehensive treatment including excited state coherences for arbitrary polarizations and magnetic field configurations is given in [22]). The Schrödinger equation for the ground state amplitudes g_m are

$$i\hbar \dot{g}_m = \sum_{m'} U_{mm'} g_{m'} \tag{14}$$

where the matrix U for the $F=3$ ground state in ^{85}Rb is given by

$$U = \hbar \frac{\chi^2}{\Delta} \begin{pmatrix} 1 & e^{ik\theta z} & 0 & 0 & 0 & 0 & 0 \\ e^{-ik\theta z} & 1 & e^{ik\theta z} & 0 & 0 & 0 & 0 \\ 0 & e^{-ik\theta z} & 1 & e^{ik\theta z} & 0 & 0 & 0 \\ 0 & 0 & e^{-ik\theta z} & 1 & e^{ik\theta z} & 0 & 0 \\ 0 & 0 & 0 & e^{-ik\theta z} & 1 & e^{ik\theta z} & 0 \\ 0 & 0 & 0 & 0 & e^{-ik\theta z} & 1 & e^{ik\theta z} \\ 0 & 0 & 0 & 0 & 0 & e^{-ik\theta z} & 1 \end{pmatrix}. \tag{15}$$

The elements of the atomic density matrix are given by $\rho_{mm'} = g_m g^*_{m'}$ where g^*_m is the complex conjugate of g_m. The rate equations for the density matrix in the m basis is given by [16]

$$i\hbar \left(\frac{\partial}{\partial t} \rho_{mm'}(z,t) + v_z \frac{\partial}{\partial z} \rho_{mm'}(z,t) \right) = \sum_{m''} U_{mm''} \rho_{m''m'}(z,t) - \sum_{m''} U^*_{m'm''} \rho_{mm''}(z,t). \tag{16}$$

For magnetic sublevels of an $F=1$ atomic system coupled by lasers with orthogonal circular polarizations, Eq. (16) reduces to Eq. (10) of Ref. [16] for a two level atom. The equations in Ref. [16] resemble the optical Bloch equations for a two level system driven by an off resonant traveling wave laser field [36].

The effect of the magnetic interaction is described by $V = g_F \mu_B \vec{\mathbf{F}} \cdot \vec{\mathbf{B}}/\hbar$ where g_F is the effective Lande g factor and μ_B is the Bohr magneton. Since the experiment considers applications relating to weak magnetic fields, we include the effect of a magnetic field by adding a term to the diagonal elements of Eq. (15) given by

$$\delta U_{mm} = \frac{g_F \mu_B B}{\hbar} m. \tag{17}$$

The initial conditions for the differential equations [Eq. (16)] depend on how the initial population is distributed among the ground state sublevels at time $t=0$ and whether there are any initial coherences. The role of optical pumping in these experiments has been pointed out in [16,22]. Experiments in trapped atoms involve excitation pulses with detunings that are large compared to the Doppler width of the sample. As a result, the effect of optical pumping during the excitation pulses is reduced. However, the strength of the MGFID and MGE can be increased by optically pumping into a particular magnetic sublevel [17]. Optical pumping into the high $|m|$ sublevels can also occur when the sample is cooled in an optical molasses [37].

Equations (14)–(16) ignore the effect of the pulse bandwidth that can result in excitation of only a fraction of the velocity distribution. In the simulations, the initial conditions assume that the atoms are optically pumped into the $F=3$, $m_F=3$ magnetic sublevel of ^{85}Rb and that there are no initial coherences. Since the coherence established by the excitation pulses is spatially modulated, we assume periodic boundary conditions on the spatial variable z for the various $\rho_{mm'}$ and solve Eq. (16) numerically for all $\rho_{mm'}$. The coherences evolve due to the interaction with the first pulse and the state of the system at $t=T$ defines the initial conditions for the interaction with the second pulse. Each $\rho_{mm'}(t)$ is then averaged over the Maxwell-Boltzmann velocity distribution to give the MGE amplitude.

The simulations show that magnetic field induced oscillations occur within the envelope of the MGE [the envelope is shown in Fig. 1(c)]. For a given polarization of the excitation pulses and a fixed magnetic field, we find that the form of the Larmor oscillations in the MGE envelope has the same functional form as the Larmor oscillations in the MGFID. Figure 4 shows the results with Lin $\perp$ Lin excitation pulses that couple magnetic sublevels with $\Delta m = 1$. In this case, Fig. 4 shows ρ_1^1 as a function of t. The magnetic field was applied along the polarization direction of $\vec{\mathbf{k}}_1$. In the context of measuring Larmor oscillations over long time scales, the MGE

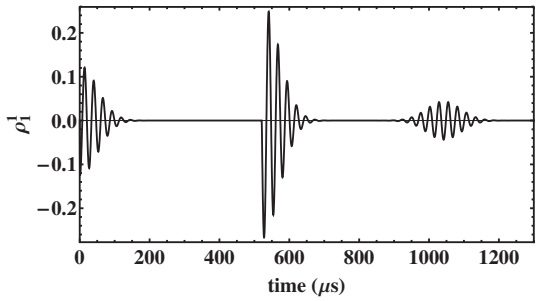

FIG. 4. Numerical solution to Eq. (16) using Lin⊥Lin excitation for $T=521.1$ μs showing the time-dependent evolution of ρ_1^1 assuming that atoms in the $F=3$ ground state are optically pumped into the $m_F=3$ sublevel. The MGFID due to each of the excitation pulses and the corresponding MGE are shown. The pulse widths of the first and second excitation pulses are 1 μs and 300 ns, respectively. The angle between excitation pulses is 25 mrad. The static magnetic field is 0.08 G along the polarization direction of $\vec{\mathbf{k}}_1$. The sample temperature was assumed to be 100 μK.

envelope can provide an enhancement in the observation time by about a factor of 2.

In the presence of a static magnetic field, it can be shown on the basis of Ref. [38] that the MGE envelope is always a maximum at $t=2T$ if the pulse separation T is changed, a result that has been verified on the basis of simulations.

We now discuss the amplitude oscillations of the entire echo envelope. Figure 5 shows simulations for laser cooled atoms for the same conditions as in Fig. 4. The simulations were carried out for values of T that are long compared to the decay time of the MGFID. The amplitude of the MGE oscillates as a function of T with a characteristic frequency $\sqrt{(\frac{\chi^2}{\Delta})^2+\omega_L^2}$. This expression has the same form as the generalized Rabi frequency for a laser field interacting with a two level atom. The term $\frac{\chi^2}{\Delta}$ characterizes the two photon interaction and replaces the one photon Rabi frequency. The two photon detuning ω_L due to the Zeeman shifted magnetic sublevels levels replaces the one photon detuning.

Simulations have also confirmed that the relative amplitudes between the primary and secondary peaks as well as the overall shape in Fig. 5 are modified by varying the length

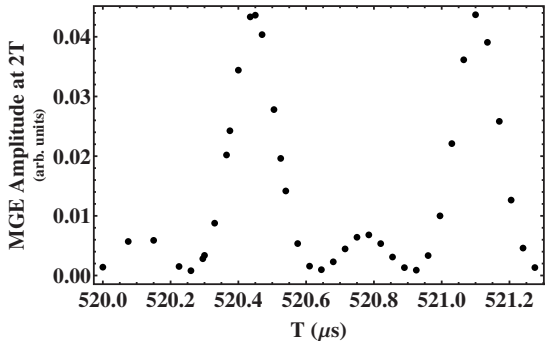

FIG. 5. Simulated MGE amplitude (at $t=2T$) using Lin⊥Lin excitation as a function of T for a laser cooled sample at a temperature of 100 μK. The magnetic field of 0.08 G was applied along one of the polarization directions. The first and second excitation pulses were 1 μs and 0.3 μs in duration. $\chi=0.3\Gamma$ and $\Delta=7\Gamma$

of the second excitation pulse. This is consistent with the expectation that an increase in the pulse area would result in couplings between adjacent magnetic sublevels across the entire $F=3$ manifold. We note that ρ_1^1 in Fig. 5 is a weighted sum of such couplings.

The simulations ignore the spatial variation in the Rabi frequency χ due to the laser beam profile. In the experiments described in Sec. IV, the excitation beams have a Gaussian spatial profile. This causes the component of the oscillation at frequency $\xi=\frac{\chi^2}{\Delta}$ to wash out on a time scale of $\sim 1/\xi$ ($\sim$100 ns). As a result, it can be expected that the frequency of the T-dependent oscillations will be ω_L if the signal is observed on a typical time scale of several milliseconds. Simulations have confirmed that the amplitude of the envelope of the MGFID due to the second excitation also exhibits similar oscillations that are $\pi/2$ out of phase with the MGE envelope oscillations (when the MGE is a maximum, the MGFID is a minimum). The simulations are consistent with expectations based on more formal considerations since Eq. (A43) of Ref. [16], derived in the limit $\chi \ll \delta$ where δ is the two photon detuning, shows that the echo envelope oscillates as a function of T with frequency δ.

The envelope oscillations can be exploited to observe Larmor oscillations on a much longer time scale (of order T) which can be comparable to the transit time for cold atoms through the region of interaction. This enhancement in the time scale can significantly improve the precision with which ω_L can be determined compared to a measurement based on recording the Larmor oscillations within the envelope of the MGFID and MGE.

The time scale on which magnetic field induced oscillations in the amplitude of the echo envelope can be observed will be limited by the presence of magnetic field gradients. In the presence of a gradient, all the atoms that contribute to the signal have slightly different Larmor frequencies, depending on their spatial locations. As T increases, the oscillations from individual atoms get out of phase and cancel out. To model this effect, we assume a functional form for the MGE amplitude to be

$$\rho_1^1 = \exp\left[-\left(\frac{(t-2T)}{\tau}\right)^2 + i\omega_L(x)(t-2T)\right]\cos[\omega_L(x)T+d], \tag{18}$$

where $\tau=\frac{2}{ku\theta}$ is the width of the echo envelope, $\omega_L(x)=\frac{g_F\mu_B B(x)}{\hbar}$ is the spatially dependent Larmor frequency and d is an offset. Here, the exponential factor models the Gaussian envelope with magnetic field induced oscillations, and the second factor models the T dependent amplitude of the signal envelope. Figure 6 shows the amplitude of the MGE envelope in a cold sample at $t=2T$ in the presence of a magnetic field gradient of 0.01 G/cm. Since the atoms in the sample have a Gaussian spatial distribution, the echo amplitude in Fig. 6 is obtained by weighting equation (18) by a Gaussian function and integrating over x. The results show that the oscillations in the MGE envelope die out on a time scale of $\sim$500 μs.

In Sec. IV C, we present evidence for magnetic field induced oscillations, within the MGE envelope, and T depen-

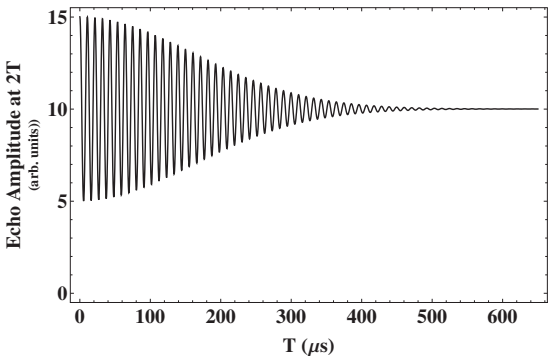

FIG. 6. Simulated MGE amplitude at $t=2T$ as a function of T in a magnetic field gradient of 0.01 G/cm. The magnetic field varies across the sample that is assumed to have a Gaussian spatial profile. The signal amplitude has contributions from atoms in a range of magnetic fields. For a T of ~ 500 μs, the oscillations are completely washed out.

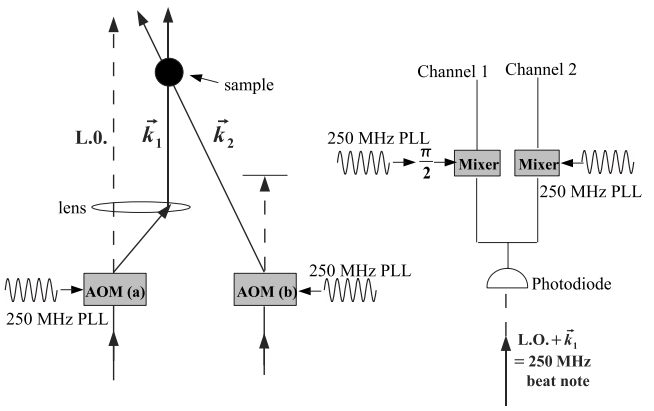

FIG. 7. Experimental setup. The AOMs are driven by a 250 MHz rf oscillator controlled by a phase locked loop (PLL). The local oscillator (L.O.) from the $\vec{\mathbf{k}}_1$ AOM is combined with the signal (MGFID, MGE) on a fast photodiode (P.D.) to produce a 250 MHz beat note which is then split into two channels. A portion of the rf at 250 MHz used to drive the AOMs is also split into two channels, with one arm $\pi/2$ out of phase with the other. The rf is mixed down to dc with the signal from the photodiode to generate the in phase and quadrature components of the signal.

dent oscillations of the amplitude of the MGE envelope and discuss improvements in the precision of g factor ratio experiments that can be realized using the echo technique.

III. EXPERIMENTAL DETAILS

The repump light resonant with the $F=2\rightarrow F'=3$ transition in ^{85}Rb is derived from a grating stabilized diode laser. The excitation pulses and atom trapping beams are derived from a Ti:Sapphire ring laser locked to the $F=3\rightarrow F'=4$ transition using saturated absorption. The saturated absorption spectrometer contains an acousto optic modulator (AOM) used as a tuning element. The AOM ensures that the portion of the laser beam going to the experiment is frequency shifted above the $F=3\rightarrow F'=4$ atomic resonance by 140 MHz. A dual pass AOM operating at $\sim$75 MHz is used to generate the light frequency shifted $\sim$12 MHz below resonance that is used for atom trapping. The portion of light 140 MHz above resonance is frequency up shifted by 150 MHz using another AOM operating in dual pass configuration. The light from this AOM is split into two orthogonal linear polarizations. The amplitude of these beams are controlled by two independent AOMs [AOM (a) and AOM (b)] that impose a frequency down shift of 250 MHz as shown in Fig. 7. The 250 MHz driving frequency is generated by a voltage controlled oscillator that is phase locked to a stable 10 MHz signal from a Rb clock. Thus the excitation beams are $\sim$40 MHz above resonance. The excitation beam radii were $\sim$5 mm for all experiments. The same arrangement can be used to trap and excite ^{87}Rb atoms by tuning the repump laser to the $F=1\rightarrow F'=2$ transition and the Ti:Saphirre laser to the $F=2\rightarrow F'=3$ transition.

The sample is excited by pulses from AOMs (a) and (b) (defined as $\vec{\mathbf{k}}_1$ and $\vec{\mathbf{k}}_2$, respectively). These pulses are aligned at an angle of $\theta\sim 10$ mrad. As a result, the MGFID and MGE signals are sensitive to the atomic velocity distribution in the direction $\vec{\mathbf{k}}_2-\vec{\mathbf{k}}_1\sim k\theta$. By using the dual pass AOM to control the envelope of the pulses going into AOMs (a) and (b), we ensure that the on and/or off ratio for light intensity is greater than 10^6. In experiments with trapped atoms, the excitation pulse bandwidths ($\sim$1 MHz) are larger than both the one photon Doppler width ($\sim ku$) and two photon Doppler width ($\sim ku\theta$). Here, $k=2\pi/\lambda$ where λ is the optical wavelength and u is the most probable speed. For experiments in room temperature vapor, the excitation pulse bandwidths are $\sim$10 MHz, which is larger than the two photon Doppler width and smaller than the one photon Doppler width. Thus a relatively narrow portion of the velocity distribution under the Doppler width of the one photon transition is excited along the direction of propagation of the excitation beams. However, all atoms moving in the transverse direction are resonant with the excitation pulses. In all experiments, the excitation pulse intensities were ~ 10 I_{sat}, where I_{sat} is the saturation intensity (assuming equally populated magnetic sublevels, $I_{sat}=7.56$ mW/cm^2 in ^{85}Rb and $I_{sat}=6.94$ mW/cm^2 in ^{87}Rb).

To detect the signal, we turn on a read out pulse along $\vec{\mathbf{k}}_2$ and detect the signal along the direction $\vec{\mathbf{k}}_1$. This involves beating the signal with an optical local oscillator [undiffracted beam from AOM (a)] on a fast photodiode and detecting a beat note at 250 MHz. The heterodyne signal can be mixed down to dc to produce the in phase and quadrature components of the signal. Some of the studies relating to the MGE from trapped atoms were carried out using counterpropagating excitation pulses. In this case, the signal intensity was measured using a gated photomultiplier tube (PMT) that was turned on just before the readout pulse.

We use a vapor cell loaded magneto optical trap [39,40] in which $\sim 10^8$ atoms are loaded in $\sim$100 ms. The atom number is inferred from fluorescence measurements using a calibrated PMT. After loading the trap, the gradient coils are turned off in $\sim$500 μs. The trapping beams are turned off in less than 100 ns and the sample temperature under these conditions is ~ 100 μK. For studies of the MGFID and MGE in

magnetic fields, the sample is further cooled in a optical molasses to temperatures below 50 μK. This involves changing the frequency of the trapping beams abruptly from a detuning of ~12 MHz below resonance to ~30 MHz below resonance. The excitation pulses are turned on after turning off the trapping beams.

For experiments carried out in room temperature vapor, the beams were aligned through a Rb cell of length 5 cm.

We record the MGFID and MGE signal envelopes using either a short (100 ns), strong ($I \gg I_{sat}$) read out pulse, or a relatively weak ($I \gg I_{sat}$) read out pulse with a duration comparable to the signal decay time. For the case of the strong read out pulse, the grating decays in ~100 ns due to spontaneous emission during the read out pulse. The delay of the read out pulse with respect to the excitation pulse is varied to record the MGFID and the MGE.

For heterodyne detection with a strong read out pulse, the sum of the squares of the in phase and quadrature components of the signal is integrated over the duration of the signal. The square root of this quantity is proportional to the electric field and defined as the signal amplitude. For PMT detection using an intense readout pulse, the signal intensity is obtained by integrating over the signal envelope.

If a weak read out pulse is used to probe the sample, the entire signal envelope is recorded on a single shot and averaged.

Two charge-coupled device (CCD) cameras are used to image the ballistic expansion of the cloud along the axial and radial directions with respect to the symmetry axis of the gradient coils [41]. The radial direction corresponds to the direction $\vec{\mathbf{k}}_1 - \vec{\mathbf{k}}_2$ defined by the excitation pulses. Thus it is possible to compare the temperature of the cloud using the decay time of the MGFID and the ballistic expansion of the cloud. For these temperature comparisons, the MGFID was recorded with the atoms optically pumped into the $F=3$ $m_F=3$ ground state [42]. Optical pumping was accomplished by using circularly polarized pulses resonant with the $F=3 \rightarrow F'=3$ and $F=2 \rightarrow F'=3$ transitions in the presence of a ~1 G quantizing field. After the atoms are pumped into the $m_F=3$ level, the system cannot absorb light from the pumping beams due to quantum mechanical selection rules. As a result, the fluorescence from the pumping beam should go to zero when the sample is optically pumped. We estimate that we were able to pump ~95% of the atoms into the $m_F=3$ level by recording the absorption spectrum of a circularly polarized probe beam resonant with the $F=3 \rightarrow F'=4$ transition. The pumping efficiency was presumably limited by the angle between the optical pumping beams and the quantizing magnetic field.

All studies of Larmor oscillations in the MGFID and MGE were carried out using static magnetic fields applied using a pair of Helmholtz coils without specific efforts to optically pump the system. For experiments in trapped atoms, partial optical pumping to the high $|m|$ sublevels occurred during the molasses cooling phase [37]. In room temperature vapor, any population imbalances were presumably the result of spontaneous emission during the excitation pulses.

IV. RESULTS AND DISCUSSION

A. Temperature measurements

To understand the dephasing time of the MGFID, we have carried out the experiment in the absence of magnetic fields. After atoms were loaded into the trap, the sample was optically pumped into a single magnetic sublevel following the procedure described in Sec. III. After optical pumping, all magnetic fields were turned off, and the sample was excited using Lin $\perp$ Lin pulses applied at a small angle as shown in Fig. 1. Figure 8(a) shows the envelope of the decay obtained using a short intense read out pulse with a variable delay with respect to the excitation pulse.

The signal decay is fit to a Gaussian form predicted by theory [16] and consistent with the simulations presented in Fig. 4 and with previous observations [17,18]. The time constant of the decay τ and the angle between the excitation beams are used to extract the most probable speed (and temperature) associated with the Maxwell-Boltzmann distribution of the cloud along the direction $\vec{\mathbf{k}}_1 - \vec{\mathbf{k}}_2$. Figure 8(b) shows the cloud radius as a function of delay time measured with respect to the turn off of the trapping lasers. The data are fit to a hyperbola and the temperature can be extracted from the knowledge of the cloud size and the delay time. A comparison of the temperature measurements using these

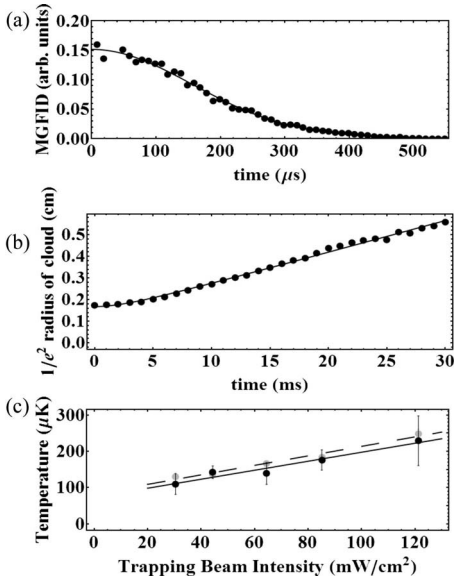

FIG. 8. (a) Decay of the MGFID (filled circles) as a function of time for an angle $\theta=6.6$ mrad. The decay time extracted by fitting the data to the equation $Ae^{-(t/\tau)^2}+C$ (solid line) gives $\tau=221$ μs. The most probable speed u given by $u=2/(k\theta\tau)$ is 0.17 m/s. The corresponding temperature is 149.2 μK. (b) Ballistic expansion of the cloud as a function of time (filled circles). u is extracted by fitting the cloud radius $R(t)$ to a hyperbola $R(t)=\sqrt{R_0^2+u^2t^2}$ (solid line) where R_0 is the initial cloud radius. (c) Temperature of the cloud measured by the CCD camera (gray scale points) and the temperature measured from the decay time of the MGFID (black filled circles) as a function of total trap laser intensity. Straight line fits are represented by the dashed line with equation $1.3I+82.6$ μK and solid line with equation $1.2I+73.3$ μK, respectively. Here I is the trapping laser intensity in mw/cm^2.

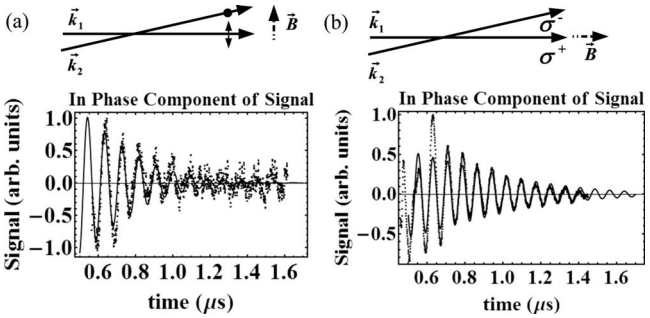

FIG. 9. Evolution of the in phase component of the MGFID in room temperature vapor. The data are shown as dots and the solid lines fits based on Eqs. (12) and (13) for Lin⊥Lin and $\sigma^+\sigma^-$ excitation, respectively. (a) The excitation pulses have orthogonal linear polarizations and the magnetic field is directed along the polarization of $\vec{\mathbf{k}}_1$; B=24.6 G; ω_L=12.13(2) MHz from the fit. (b) The excitation pulses have opposite circular polarizations with the direction of the magnetic field along $\vec{\mathbf{k}}_1$; B=12 G; and the oscillation frequency of 13.081(8) MHz is $2\omega_L$, consistent with expectations. For both (a) and (b), the excitation pulse widths were 100 ns, and the one photon detuning was 40 MHz. The cell length is 5 cm.

two techniques is shown in Fig. 8(c). The temperature was varied by changing the total trap laser intensity. It is clear that the temperature measurements show good agreement within experimental error. Both methods establish the linear dependence of temperature on trap laser intensity which is a signature of polarization gradient cooling [41,43].

B. Evolution of MGFID in magnetic fields

In a uniform static magnetic field, the MGFID is probed using a long weak read out pulse to record the entire decay in a single shot. Figure 9(a) shows an average over 256 repetitions of the MGFID in a room temperature vapor cell when a magnetic field is applied along the direction of polarization of $\vec{\mathbf{k}}_1$ for Lin⊥Lin excitation. The Doppler dephasing time is ~ 1 μs which is consistent with the room temperature velocity distribution. For this geometry, the MGFID is proportional to the irreducible tensor element ρ_1^1. Setting $\eta=0$ in Eq. (12) gives $\rho_1^1 \propto e^{i\omega_L t}$. The functional form of the in phase and quadrature components of the signal are predicted to have a sinusoidal dependence with oscillation frequency ω_L. For $\sigma^+\sigma^-$ excitation, and a magnetic field along $\vec{\mathbf{k}}_1$, Eq. (13) with $\eta=0$ reduces to $\rho_2^2 \propto e^{i2\omega_L t}$. In this case, the MGFID oscillation frequency is predicted to be $2\omega_L$. The data in Fig. 9 shows that fits based on these theoretical expressions accurately model the signal shapes of the in phase component of the signal (the quadrature component which is phase shifted by $\pi/2$ is not shown). The data also confirms the predicted oscillation frequency.

Figure 10 shows the MGFID with the magnetic field at an angle $\eta=\pi/4$ in room temperature vapor. Both the in phase and quadrature components of the signal are shown for Lin⊥Lin and $\sigma^+\sigma^-$ excitation and show that the evolution exhibits more Fourier components. For Lin⊥Lin excitation, Eq. (12) reduces to $\rho_1^1 \propto i\{2\cos[\omega_L t]+\sqrt{2}(1+i\sin[\omega_L t])\}$ whereas for $\sigma^+\sigma^-$ excitation, Eq. (13) reduces to $\rho_2^2 \propto 3(1+\frac{4}{3}\sqrt{2}\cos[\omega_L t]+\cos[2\omega_L t])+2i(2\sin[\omega_L t]+\sqrt{2}\sin[2\omega_L t])$. Data shown in Fig. 10 agree with the fits based on the theoretical prediction for ρ_1^1 and ρ_2^2. The overall signal shapes are consistent with predictions. The discrepancy for $t>1$ μs is attributed to the presence of magnetic field gradients.

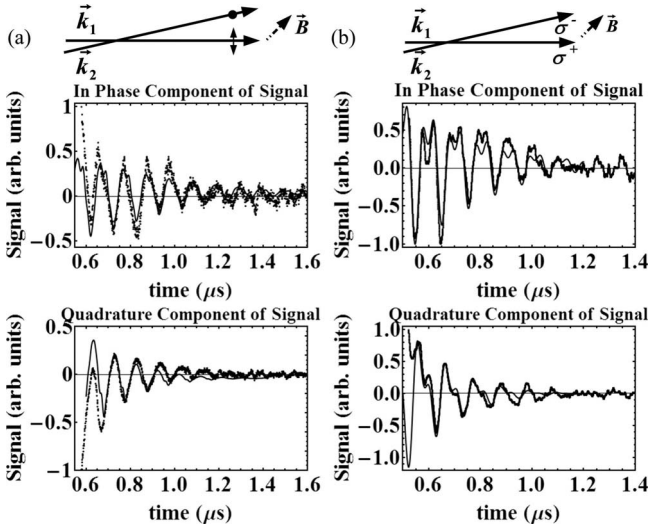

FIG. 10. Evolution of the in phase and quadrature parts of the MGFID in room temperature vapor. The data are shown as dots and the solid lines fits based on Eqs. (12) and (13) for Lin⊥Lin and $\sigma^+\sigma^-$ excitation, respectively. (a) The excitation pulses have orthogonal linear polarizations and the magnetic field is directed at an angle of $\frac{\pi}{4}$ with respect to the polarization of $\vec{\mathbf{k}}_1$. (b) The excitation pulses have opposite circular polarizations with the direction of the magnetic field at an angle of $\frac{\pi}{4}$ to the direction of $\vec{\mathbf{k}}_1$. In both cases the excitation pulse widths were 100 ns, and the detuning was 40 MHz. The cell length is 5 cm.

In laser cooled atoms, the effect of a magnetic field gradient is expected to be highly suppressed due to the compact dimensions of the sample (a few millimeters) and the magnetic field is more uniform. However, the effect of the gradient can become more pronounced over long time scales. The complicated evolution of the coherences can be observed clearly as illustrated in Fig. 11 which shows the MGFID from trapped atoms for the same magnetic field configuration as in Fig. 10 for both Lin⊥Lin and $\sigma^+\sigma^-$ excitation. The Larmor oscillations can be recorded over time scales that are ~100 times larger than in room temperature vapor because of the narrow Doppler width. As a result, the experiment is suitable for precision measurements.

C. Applications to precision measurements of *g* factor ratios

The relatively long decay time of the MGFID and the ability to apply a uniform magnetic field across a compact sample suggests that this technique may be suitable for precision measurements of magnetic interactions such as atomic *g* factor ratios and Zeeman shifts. It is interesting to note that the most precise examples of such measurements (at the level of a few parts per 10^6) were carried out several decades ago [12,13] using rf spectroscopy and optical pumping and measuring line shapes in atomic vapor in the presence of

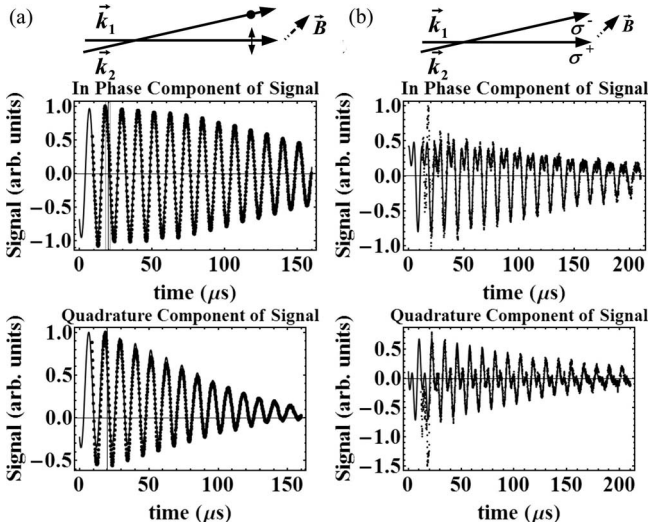

FIG. 11. Evolution of the in phase and quadrature parts of the MGFID in a sample of cold atoms. (a) The excitation pulses have orthogonal linear polarizations and the magnetic field is directed at an angle of $\frac{\pi}{4}$ with respect to the polarization of $\vec{\mathbf{k}}_1$. (b) The excitation pulses have opposite circular polarizations with the direction of the magnetic field at an angle of $\frac{\pi}{4}$ to the direction of $\vec{\mathbf{k}}_1$. In both cases the excitation pulse widths were 2 μs, and the detuning was 40 MHz. The data are shown as dots and the solid lines fits based on Eqs. (12) and (13).

static magnetic fields. In this section, we discuss the possibility of improving the precision associated with the measurement of atomic g factor ratios using the behavior of the MGFID and MGE in magnetic fields [14,15].

Figure 12 shows the MGFID from trapped ^{85}Rb atoms averaged over 256 repetitions on a time scale of ~1 minute. Lin $\perp$ Lin excitation pulses at an angle of a few milliradians and a static magnetic field of ~0.3 G were used. Figure

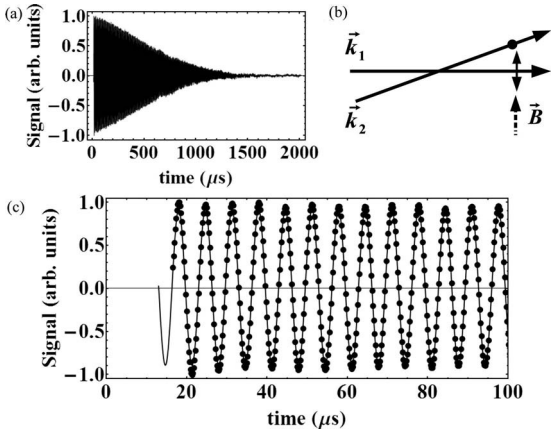

FIG. 12. In phase component of the MGFID with Lin $\perp$ Lin. excitation in a weak magnetic field of ~0.3 G and a detuning of $\Delta=40$ MHz above the $F=3\rightarrow F'=4$ resonance. (a) Entire signal envelope. (b) Excitation geometry showing the magnetic field to be along one of the polarization directions. (c) Expanded view of the signal in (a) show data (dots) and fit (solid line). From a fit to a decaying sine wave, the frequency is $\nu_L=0.150\,688\,0(6)$ MHz. The fit is based on Eq. (12).

12(a) shows the overall signal decay on a time scale of over 1 ms using a sample cooled to ~50 μK. Figure 12(b) shows the geometry of the experiment. For this configuration, the evolution of the MGFID is purely sinusoidal as shown in Fig. 12(c).

To determine the oscillation frequency, the data is fit to a function based on Eq. (12) with $\eta=0$. The fit yields a $\nu_L=0.1506880(6)$ MHz [~4 parts per 10^6 (ppm)] where, $\nu_L=\omega_L/(2\pi)$. After recording this data, the frequency of the trapping lasers were switched to trap ^{87}Rb. The laser frequencies were switched within ~1 minute, and the MGFID experiment was repeated with comparable precision using the $F=2\rightarrow F'=3$ resonance in ^{87}Rb. Thus it was possible to measure the ratio of Larmor frequencies. From the measurements in the two isotopes, the g factor ratio $\frac{g_{F_{87}}}{g_{F_{85}}}$, which is the ratio of Larmor frequencies, was determined to a precision of ~10 ppm. Here, g_F is the effective Landé g factor given by

$$g_F = g_J \frac{F(F+1)+J(J+1)-I(I+1)}{2F(F+1)} - g_I \frac{F(F+1)+I(I+1)-J(J+1)}{2F(F+1)}, \tag{19}$$

where g_J contains the electron g factor, and g_I is the nuclear g factor. The absolute value of the measured g factor ratio is not stated since the accuracy is affected by time varying magnetic fields. It is therefore crucial to ensure that variations in the magnetic field are eliminated during the time in which the Larmor frequency measurements are recorded for the two isotopes.

Measurements that are in progress are investigating systematic effects by using active field cancelation to limit the fluctuations in the magnetic field, and magnetic shielding to reduce magnetic field gradients. In these experiments, the rotation matrix approach developed in this work plays an important role in correcting the effects of small changes in the direction of the magnetic field on the observed signal shape. Improvements in precision can be achieved using smaller angles between excitation pulses so that the signal decays on a longer time scale. Our results suggest that a precision of ~500 parts per 10^9 (ppb) may be attainable using this technique.

We now discuss the possibility of further increasing the precision using the MGE. This raises the exciting prospect of testing relativistic effects that have been predicted at the level of 100 ppb by Ref. [11]. Following the discussion in Sec. II D, we first discuss the improvement related to observing oscillations within the echo envelope, and then discuss the much more significant improvement (about a factor of 10) that can be realized by observing T dependent oscillations in the amplitude of the echo envelope.

Figure 13 shows Larmor oscillations in the MGE for $T=700$ μs for the same configuration as in Fig. 12. The MGFID due to the second excitation pulse and the echo in the vicinity of $t=2T$ are shown. Both the MGFID and the MGE are probed by a weak ($I \ll I_{sat}$) read out pulse whose duration extends from the end of the second excitation to well beyond the duration of the MGE envelope. Magnetic field oscilla-

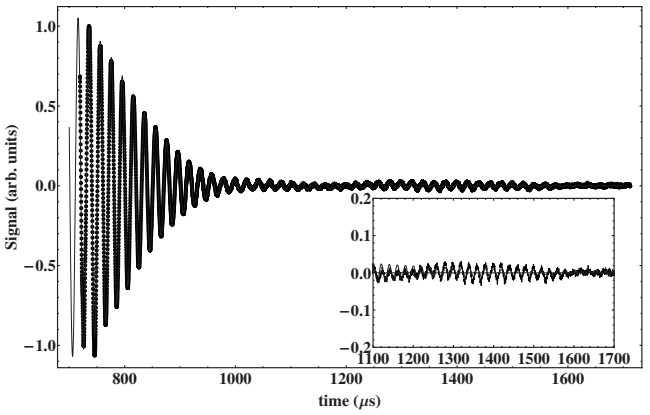

FIG. 13. Data showing Larmor oscillations in the MGFID due to the second excitation pulse at $T=700$ μs and Larmor oscillations in the echo envelope at $t=2T$ (1400 μs). The excitation pulses had orthogonal linear polarizations and the magnetic field was ~0.1 G. The lengths of the first and second pulses were 2 μs and 300 ns, respectively. The inset shows and expanded view of the Larmor oscillations in the echo envelope. A fit based on Eq. (12) gives ν_L =0.051 62(4) MHz. Both the MGFID and MGE exhibit Larmor oscillations with the same functional form. The results are consistent with simulations in Fig. 4.

tions in the echo envelope are also shown in the inset. A Gaussian fit to the echo envelope confirms that its decay time is comparable to the decay time of the MGFID. The data confirms the theoretical prediction in Fig. 4 based on the rate Eqs. (14)–(16) and shows that the magnetic field oscillations in the MGFID and the MGE have the same functional form. A fit to the data in the inset shows that the precision in ω_L is improved by a factor of 1.5 in comparison to the fit to the MGFID. It could be expected that the increase in precision should be proportional to the increase in time scale (~2). However, the signal to noise is reduced if the MGE is recorded by a weak read out pulse. This effect can be avoided by using an intense read out pulse as in the figures related to the following discussion.

Figure 14 shows the amplitude of the MGE at $t=2T$ as a function of T from trapped atoms with the excitation pulses detuned by 19 MHz with respect to the excited state. This data was obtained using a strong short read out pulse. To record MGE signals for small values of T, we used counter-propagating excitation pulses ($\vec{\mathbf{k}}_1 \approx -\vec{\mathbf{k}}_2$) so that durations of the MGFID and MGE envelopes are ~1 μs. As a result, the MGE amplitude could be recorded within a few microseconds after the excitation pulses.

As shown in Fig. 14, the time scale over which the magnetic field induced amplitude oscillations of the MGE envelope could be observed was limited by the presence of magnetic field gradients of ~0.01 G/cm due to the magnetized walls of the stainless steel vacuum chamber [44].

For this geometry, the effect of atomic recoil is significant. A full fledged calculation of the signal is very different from the calculations of the MGFID and MGE carried out in this work as well as in Ref. [16] and beyond the scope of this paper. For this reason, the results can only be compared qualitatively with the simulations presented in Fig. 5. The signal amplitude in Fig. 14 shows the expected modulation at

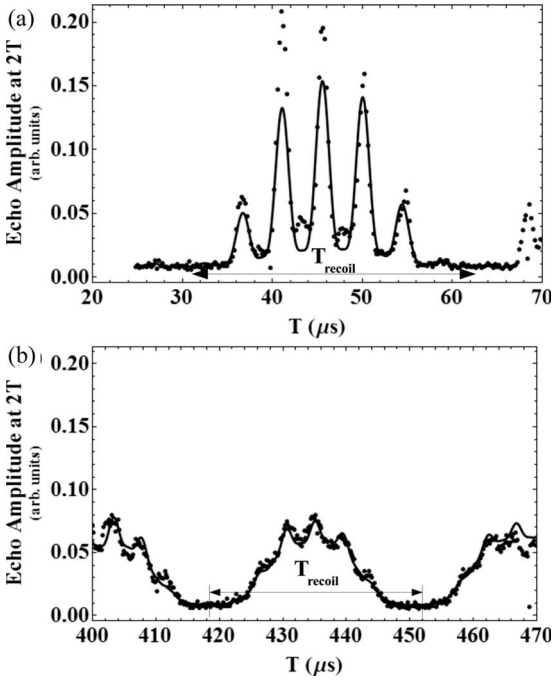

FIG. 14. MGE signal intensity measured with a PMT (dots) using counter-propagating Lin⊥Lin excitation pulses in a laser cooled sample. A magnetic field of $B \sim 0.25$ G is directed along the polarization direction of $\vec{\mathbf{k}}_1$. The first and second excitation pulses are 680 ns and 70 ns in duration, respectively. In addition to the T-dependent magnetic field oscillations, the signal is modulated at the atomic recoil frequency [ω_r=0.096 95(4) MHz]. The data are fit to the functional form of Eq. (26) in Ref. [28] with an additional $\cos^4[\omega_L T]$ term to account for the magnetic field oscillations (solid line). The extracted value of ω_L is consistent with the expected value.

the atomic recoil frequency $\omega_r = \frac{\hbar(\Delta k)^2}{2M_{\mathrm{Rb}}}$ where $\hbar\Delta k = \hbar|\vec{\mathbf{k}}_1 - \vec{\mathbf{k}}_2|$ is the momentum transfer to the atoms from the laser fields and M_{Rb} is the atomic mass. The corresponding value of T_{recoil} shown in Fig. 14 is ~32 μs ($T_{recoil} = \pi/\omega_r$). ω_L was determined to be 0.110 395(15) MHz (~100 ppm) from a fit based on Eq. (26) in Ref. [28] with an additional $\cos^4[\omega_L T]$ term to account for the magnetic field oscillations. The value of ω_L was consistent with expectations based on the applied magnetic field. Both ω_r and ω_L were obtained from a single multiparameter fit to the data in Figs. 14(a) and 14(b).

Figure 14(b) shows that the Larmor oscillations in the amplitude of the echo envelope cancel out for $T \sim 500$ μs although the overall decay time of the signal is several milliseconds. The effect of the magnetic gradient is consistent with the expectations based on Fig. 6. The gradient can be greatly reduced by carrying out the experiment in a magnetically shielded glass chamber. Gradients are also known to limit the overall lifetime of the MGE (the time T in which the signal amplitude reduces to half its initial value). For these experiments, the lifetime was ~2.4 ms, whereas the lifetime can be as large as the transit time of cold atoms through the region of interaction defined by the excitation pulses [45]. As a result, it is clear that further improvements in the precision of the g factor ratio can be expected by utilizing the MGE. For a sample temperature of ~50 μK and

an excitation beam diameter of a few centimeters, the expected lifetime is ~100 ms with the excitation beams aligned along the vertical. If these excitation beams are aligned along the horizontal, the time scale on which atoms would leave the interaction region due to gravity is ~45 ms. The experiments in Refs. [46,47] are recent examples in which the Larmor frequency has been measured using the Faraday effect and in these experiments, the effect of gravity was avoided by using dipole force traps and optical lattices. Another approach for reducing transit time losses due to gravity involves aligning the excitation beams along the vertical. The small angle between the beams ensures a large region of overlap. Under these conditions, we estimate that the MGE oscillation frequency can be measured to a precision of ~50 ppb by recording temporally separated Larmor oscillations. The time to acquire this data is expected to be ~1 hour.

V. CONCLUSIONS

We have shown that the MGFID can be used for accurate measurements of the velocity distribution. Such measurements have applications for phase space imaging [31,48]. We have developed a general theoretical frame work for predicting the evolution of magnetic sublevel coherences in arbitrary static magnetic fields. The theoretical predications are consistent with experiments that investigated the properties of the MGFID in room temperature vapor and laser cooled samples. For particular configurations of excitation pulses and magnetic fields, the results also agree with previous observations [17]. Data in Fig. 11 suggests that the effect of magnetic field gradients can be reduced by using a compact sample. We have established that Larmor oscillations in the MGFID could be used for a precise determination of the atomic g factor ratio.

Simulations of the MGE show that a magnetic field produces Larmor oscillations under the envelope that have the same functional form as the oscillations in the MGFID. These oscillations are predicted to have the same frequency as the oscillations in the amplitude of the MGE envelope as a function of T. The experimental results have confirmed these predictions and established that the MGE can potentially be exploited for achieving a significantly improved measurement of the atomic g factor ratio. Future work associated with the MGFID and the MGE could also include independent measurements of the Zeeman shift using a calibrated sensor that can be placed at the location of the trapped atomic cloud. Results of this work could be applied to observe nonlinear spectroscopic signatures predicted in [23].

ACKNOWLEDGMENTS

This work was supported by Canada Foundation for Innovation, Ontario Innovation Trust, Photonics Research Ontario, Ontario Centers of Excellence, Natural Sciences and Engineering Research Council of Canada, and York University. We acknowledge the contributions of Andrejs Vorozcovs who implemented the data acquisition programs. We would also like to thank Paul Berman of the University of Michigan for helpful discussions.

[1] G. A. Smith, A. Silberfarb, I. H. Deutsch, and P. S. Jessen, Phys. Rev. Lett. **97**, 180403 (2006).
[2] I. H. Deutsch and P. S. Jessen, Phys. Rev. A **57**, 1972 (1998).
[3] J. M. Geremia, J. K. Stockton, and H. Mabuchi, Phys. Rev. Lett. **94**, 203002 (2005).
[4] S. Chaudhury, G. A. Smith, K. Schulz, and P. S. Jessen, Phys. Rev. Lett. **96**, 043001 (2006).
[5] S. J. van Enk, N. Ltkenhaus, and H. J. Kimble, Phys. Rev. A **75**, 052318 (2007).
[6] M. Vengalattore, J. M. Higbie, S. R. Leslie, J. Guzman, L. E. Sadler, and D. M. Stamper-Kurn, Phys. Rev. Lett. **98**, 200801 (2007).
[7] Chr. Tamm, E. Buhr, and J. Mlynek, Phys. Rev. A **34**, 1977 (1986).
[8] E. Buhr and J. Mlynek, Phys. Rev. A **36**, 2684 (1987).
[9] D. Suter, M. Rosatzin, and J. Mlynek, Phys. Rev. Lett. **67**, 34 (1991).
[10] D. Suter, H. Klepel, and J. Mlynek, Phys. Rev. Lett. **67**, 2001 (1991).
[11] J. M. Anthony and K. J. Sebastian, Phys. Rev. A **49**, 192 (1994).
[12] C. W. White, W. M. Hughes, G. S. Hayne, and H. G. Robinson, Phys. Rev. **174**, 23 (1968).
[13] C. Cohen-Tannoudji and A. Kastler, in *Progress in Optics*, edited by E. Wolfe (North Holland, Amsterdam, 1966), Vol. V.
[14] I. Chan, M. Weel, S. Beattie, E. Rotberg, A. Vorozcovs, A. Andreyuk, and A. Kumarakrishnan, Bull. Am. Phys. Soc. **50**, 44 (2005).
[15] I. Chan, S. Beattie, and A. Kumarakrishnan, Bull. Am. Phys. Soc. **51**, 156 (2006).
[16] B. Dubetsky and P. R. Berman, Laser Phys. **4**, 1017 (1994).
[17] A. Kumarakrishnan, S. B. Cahn, U. Shim, and T. Sleator, Phys. Rev. A **58**, R3387 (1998).
[18] A. Kumarakrishnan, U. Shim, S. B. Cahn, and T. Sleator, Phys. Rev. A **58**, 3868 (1998).
[19] B. W. Shore, *The Theory of Coherent Atomic Excitation* (Wiley, New York, 1990), Ch 18.5.
[20] A. R. Edmonds, *Angular Momentum in Quantum Mechanics* (Princeton University Press, Princeton, 1996).
[21] S. M. Rochester and D. Budker, Am. J. Phys. **69**, 450 (2001).
[22] P. R. Berman, G. Rogers, and B. Dubetsky, Phys. Rev. A **48**, 1506 (1993).
[23] P. R. Berman, Phys. Rev. A **43**, 1470 (1991).
[24] C. Cohen-Tannoudji, J. DuPont-Roc, S. Haroche, and F. Laloë, Phys. Rev. Lett. **22**, 758 (1969).
[25] E. A. Rotberg, B. Barrett, S. Beattie, S. Chudasama, M. Weel, I. Chan, and A. Kumarakrishnan, J. Opt. Soc. Am. B **24**, 671 (2007).
[26] S. B. Cahn, A. Kumarakrishnan, U. Shim, T. Sleator, P. R. Berman, and B. Dubetsky, Phys. Rev. Lett. **79**, 784 (1997).

[27] M. Weel and A. Kumarakrishnan, Phys. Rev. A **67**, 061602(R) (2003).
[28] S. Beattie, B. Barrett, M. Weel, I. Chan, C. Mok, S. B. Cahn, and A. Kumarakrishnan, Phys. Rev. A **77**, 013610 (2008).
[29] A. Kumarakrishnan, A. Karpf, Z. Khaliq, D. V. Strekalov, A. V. Turlapov, and T. Sleator, Bull. Am. Phys. Soc. **43**, 1296 (1998).
[30] U. Shim, A. Kumarakrishnan, S. B. Cahn, and T. Sleator, *Quantum Electronics Conference (IQEC)*, 1998 OSA Technical Digest Series (IEEE, Piscataway, NJ, 1998), p. 201.
[31] S. B. Cahn, A. Kumarakrishnan, U. Shim, and T. Sleator, Bull. Am. Phys. Soc. **42**, 1057 (1997).
[32] D. V. Strekalov, Andrey Turlapov, A. Kumarakrishnan, and Tycho Sleator, Phys. Rev. A **66**, 023601 (2002).
[33] A. Turlapov, A. Tonyushkin, and T. Sleator, Phys. Rev. A **68**, 023408 (2003).
[34] A. Turlapov, A. Tonyushkin, and T. Sleator, Phys. Rev. A **71**, 043612 (2005).
[35] A. Tonyushkin and T. Sleator, Phys. Rev. A **74**, 053615 (2006).
[36] L. Allen and J. H. Eberly, *Optical Resonance and Two-Level Atoms* (Courier Dover, New York, 1987).
[37] C. G. Townsend, N. H. Edwards, C. J. Cooper, K. P. Zetie, and C. J. Foot, A. M. Steane, P. Szriftgiser, H. Perrin, and J. Dalibard, Phys. Rev. A **52**, 1423 (1995).
[38] J.-L. Le Gouët and P. R. Berman, Phys. Rev. A **20**, 1105 (1979).
[39] E. L. Raab, M. Prentiss, A. Cable, S. Chu, and D. E. Pritchard, Phys. Rev. Lett. **59**, 2631 (1987).
[40] C. Monroe, W. Swann, H. Robinson, and C. Wieman, Phys. Rev. Lett. **65**, 1571 (1990).
[41] A. Vorozcovs, M. Weel, S. Beattie, S. Cauchi, and A. Kumarakrishnan, J. Opt. Soc. Am. B **22**, 943 (2005).
[42] K. E. Gibble, S. Kasapi, and S. Chu, Opt. Lett. **17**, 526 (1992).
[43] J. Dalibard and C. Cohen-Tannoudji, J. Opt. Soc. Am. B **6**, 2023 (1989).
[44] M. Weel, I. Chan, S. Beattie, A. Kumarakrishnan, D. Gosset, and I. Yavin, Phys. Rev. A **73**, 063624 (2006).
[45] I. Yavin, M. Weel, A. Andreyuk, and A. Kumarakrishnan, Am. J. Phys. **70**, 149 (2002).
[46] M. L. Terraciano, M. Bashkansky, and F. K. Fatemi, Phys. Rev. A **77**, 063417 (2008).
[47] G. A. Smith, S. Chaudhury, and P. S. Jessen, J. Opt. B: Quantum Semiclassical Opt. **5**, 323 (2003).
[48] J. E. Thomas and L. J. Wang, Phys. Rep. **262**, 311 (1995).